

Accelerated Article Preview

Bulk superconductivity near 40 K in hole-doped SmNiO_2 at ambient pressure

Received: 17 February 2024

S. Lin Er Chow, Zhaoyang Luo & A. Ariando

Accepted: 13 March 2025

Accelerated Article Preview



Cite this article as: Chow, S. L. E. et al. Bulk superconductivity near 40 K in hole-doped SmNiO_2 at ambient pressure. *Nature* <https://doi.org/10.1038/s41586-025-08893-4> (2025)

This is a PDF file of a peer-reviewed paper that has been accepted for publication. Although unedited, the content has been subjected to preliminary formatting. Nature is providing this early version of the typeset paper as a service to our authors and readers. The text and figures will undergo copyediting and a proof review before the paper is published in its final form. Please note that during the production process errors may be discovered which could affect the content, and all legal disclaimers apply.

1 **Bulk superconductivity near 40 K in hole-doped SmNiO₂ at ambient pressure**

2 S. Lin Er Chow,^{1✉} Zhaoyang Luo,¹ A. Ariando^{1✉}

3 ¹*Department of Physics, Faculty of Science, National University of Singapore, Singapore 117551, Singapore*

4 [✉]Corresponding author: le.chow@u.nus.edu, ariando@nus.edu.sg

5

6 **The discovery of superconductivity in the Ba-La-Cu-O system (the cuprate) in the 30 K range**
7 **marked a significant breakthrough, which inspired extensive explorations of oxide based layered**
8 **superconductors to identify electron pairing with higher critical temperatures (T_c)¹. Despite recent**
9 **observations of superconductivity in nickel-oxide-based compounds (the nickelates), evidence of**
10 **Cooper pairing above 30 K in a system that is isostructural to the cuprates, but without copper, at**
11 **ambient pressure and without lattice compression, has remained elusive^{2–5}. Here, we report**
12 **superconductivity with a T_c approaching 40 K under ambient pressure in the d^{9-x} hole-doped, late**
13 **rare-earth infinite-layer nickel oxide (Sm-Eu-Ca-Sr)NiO₂ thin films with negligible lattice**
14 **compression, supported by observations of a zero resistance state at 31 K and the Meissner effect.**
15 **The material can be synthesized with essentially no Ruddlesden-Popper type structural defects,**
16 **exhibiting ultralow resistivity of ~ 0.01 mΩ · cm with a residual-resistivity-ratio of up to 10. Our**
17 **findings demonstrate the potential of achieving high-temperature superconductivity using strongly**
18 **correlated d -electron metal oxides beyond copper as the building blocks for superconductivity,**
19 **offering a promising platform for further exploration and understanding of high-temperature**
20 **Cooper pairing.**

21

22

23 **Main**

24 A longstanding question in condensed matter physics is whether high-temperature (high- T_c)
25 superconductivity above 30 K at ambient pressure is unique to quasi-two-dimensional copper oxides
26 (cuprates)¹ or if it is ubiquitous among transition metal layered oxides in the periodic table of elements^{6–8}.
27 Following Bednorz and Müller's success with copper oxides¹, intense efforts into the realization of
28 analogous high- T_c Cooper pairing in non-copper oxides have been undertaken for more than three
29 decades^{1–3,9–12}. This pursuit eventually led to the successful realization of superconductivity in nickel
30 oxides (nickelates) with a $T_c \sim 15$ K^{1,4,13–15}. Subsequently, a family of d^{9-x} infinite-layer (La/Pr/Nd)NiO₂
31 and quintuple layer Nd₆Ni₅O₁₂ nickelates have been studied^{4,15–21}. In addition, under lattice compression
32 by high-pressure or compressive strain, high-temperature superconductivity can be observed in $d^{7+\alpha}$
33 occupancy of nickel in the Ruddlesden–Popper nickelates^{5,22}. Several intriguing similarities and
34 differences compared to the cuprates have been reported. For example, long-range charge and spin
35 orderings have yet to be conclusively demonstrated in the hole-doping-dependent phase diagram of d^{9-x}
36 nickelates^{23–25}. Within the superconducting dome, high-field transport studies on the hole-doped
37 (La/Pr/Nd)NiO₂ show a drastic difference in the scale of upper critical fields among the various rare-earth
38 nickelates. A large Pauli-limit violation in all directions is observed in Ca/Sr-doped LaNiO₂ (refs.^{26,27}), but
39 it is absent in the Nd-nickelates counterpart^{26,28}. Meanwhile, studies of low-temperature penetration depth
40 and superfluid density studies suggest a nodal gap in the La/Pr-nickelates, but a nonzero gap minimum in
41 the Nd-nickelates^{29,30}. Further exploration of the strongly-correlated system and the nature of
42 unconventional high- T_c Cooper pairing^{31–41}, therefore demands an expansion of the superconducting
43 family and an elevation of the superconducting T_c beyond 30 K.

44

45

46

47 **Materials approach**

48 In the case of high- T_c cuprates, the largest rare-earth (La^{3+}) compound, $\text{La}_{2-x}\text{Ce}_x\text{CuO}_{4+\delta}$, has a $T_c \sim 30$ K,
49 whereas the smaller rare-earth compound, $\text{Eu}_{2-x}\text{Ce}_x\text{CuO}_{4+\delta}$, has a lower $T_c \sim 10$ K (ref⁴²). For the d^{9-x}
50 infinite-layer nickelates, the crossing rare-earth 5d bands and their three-dimensional electronic structures
51 mark the first deviation from the cuprates' quasi-two-dimensional single-band picture^{14,34-37,43}. It is
52 therefore critical to evaluate the rare-earth dependence of superconducting T_c , phase diagram,
53 dimensionality, order parameter, Fermi surfaces, symmetries, and competing orderings of the strongly-
54 correlated nickelates^{25,33,39,41,44}. From this perspective, samarium-nickelate is the next logical candidate to
55 expand the rare-earth families. Moreover, our previous work on the dimensionality manipulation of
56 superconductivity in the infinite-layer nickelates⁴⁵ suggested that the later rare earth ions in the spacer layer,
57 when substituted with smaller cations such as Ca^{2+} or $\text{Eu}^{2+/3+}$, might lead to stronger interlayer hopping and
58 interactions that may be pertinent to superconducting coupling, and new unconventional phases.
59 Considering that Sr^{2+} , Ca^{2+} and $\text{Eu}^{2+/3+}$ ions have been established as effective hole dopants^{4,16,19,31,46,47}, we
60 propose a general formula for hole-doped late rare earth samarium-nickelate: $\text{Sm}_{1-x-y-z}\text{Eu}_x\text{Ca}_y\text{Sr}_z\text{NiO}_2$
61 (SECS) infinite-layer nickelates. The crystal structure of this superconducting candidate is schematically
62 illustrated in **Fig. 1a**.

63

64 **High crystalline $\text{Sm}_{1-x-y-z}\text{Eu}_x\text{Ca}_y\text{Sr}_z\text{NiO}_2$ (SECS) thin films**

65 Here, we synthesized a series of SECS nickelate thin films stabilized on $\text{NdGaO}_3(110)$ substrate with
66 various doping compositions. **Figure 1b** shows the X-ray diffraction pattern of a representative
67 superconducting SECS thin film, $\text{Sm}_{0.79}\text{Eu}_{0.12}\text{Ca}_{0.04}\text{Sr}_{0.05}\text{NiO}_2$. Laue fringes are visible. The infinite-layer
68 phase is identified with an interplanar distance calculated to be ~ 3.27 Å from the (002) peak position,
69 which is consistent with the theoretical values for tetragonal $P4/mmm$ space group⁴⁸. The high crystalline
70 quality is further visualised using cross-sectional scanning transmission electron microscopy (STEM) high-

71 angle annular dark field (HAADF) imaging, as shown in **Fig. 1c** and **Extended Data Fig. 1,2**. Virtually
72 no Ruddlesden–Popper (RP) type stacking faults are observed throughout the entire sample volume.
73 Evidently, a uniform infinite-layer lattice without structural RP type defects can be achieved in SECS
74 infinite-layer nickelate, making it a promising and reliable platform for further experimental studies on the
75 intrinsic orderings and phases of strongly correlated nickelate superconductors.

76

77 **Transport properties**

78 **Figures 2a-c** shows the resistivity $\rho(T)$ curves of several representative superconducting SECS nickelate
79 thin films with various doping compositions. All the $\rho(T)$ curves exhibit a T -linear dependence at high
80 temperatures, followed by a positive curvature indicative of non-Fermi-liquid $T^{1 < n < 2}$ dependence at lower
81 temperatures. **Extended Data Fig. 3** plots the curvature $\frac{\partial^2 \rho}{\partial T^2}$ of the resistivity $\rho(T)$ curve shown in **Fig. 2b**.
82 The curvature becomes negative as the resistivity drops where superconductivity emerges. In comparison,
83 for the higher hole doping outside of the superconducting phase, such as in the overdoped $h = 0.31$
84 $\text{Sm}_{0.53}\text{Eu}_{0.4}\text{Ca}_{0.07}\text{NiO}_2$ (**Extended Data Fig. 4**), curvature $\frac{\partial^2 \rho}{\partial T^2} \geq 0$ at all temperatures. The transport
85 behaviour is similar except without a resistivity drop, remaining completely metallic with a low residual
86 resistivity on the order of $10 \mu\Omega \cdot \text{cm}$ and a residual-resistivity-ratio (RRR) ~ 10 . The low residual
87 resistivity (and high RRR) might be partially attributed to the small variance in the A-site spacer-layer
88 ionic radii⁴⁹. Therefore, Ca/Eu-doped SmNiO_2 could be an ideal platform to investigate the intrinsic phase
89 diagram of the infinite-layer nickelates under various control parameters such as doping, pressure, strain,
90 and fields. For superconducting dopings, their resistivity curvatures are non-negative before the
91 superconducting transition, where the resistivity drops to zero at temperatures up to $\sim 31 \text{ K}$ (**Fig. 3a**). The
92 zero resistance state $T_{c,0} = 31 \text{ K}$ marks not only a new record for infinite-layer nickelates but also the first
93 non-copper oxide whose zero resistance state temperature surpasses 30 K at ambient pressure^{2,3,50}. The
94 superconducting phase in SECS is highly reproducible and relatively stable under ambient environment

95 (refer to Supplementary Information Fig. S1,S2 and Table S1,S2 for the additional information on the
96 superconducting transition in the SECS nickelates).

97

98 **Meissner state of the superconducting nickelate thin films**

99 Together with the robust zero resistance state, evidence of the Meissner effect is unambiguously
100 demonstrated in **Fig. 3b** and **Figs. 4a,b**, which completes the puzzle of the bulk superconducting nature of
101 SECS and the related family of superconducting nickelate thin films. We observed a substantial
102 diamagnetism below $T_{c,\chi} \sim 27$ K from the zero-field cooling DC susceptibility measurements (**Fig. 3b**),
103 despite the few nm ultrathin superconducting film and a large positive paramagnetic background from the
104 500 micron-thick NGO substrates (refer to the raw data in **Extended Data Fig. 5** and Supplementary
105 Information Fig. S3). The unequivocal Meissner state is demonstrated in the field dependence
106 susceptibility M - H curve as shown in **Fig. 4**. A negative M - H slope is observed near zero field (**Fig. 4a**),
107 implying a complete field expulsion below T_c , emphasizing the strong superconducting phase homogeneity
108 in the nickelate thin films. Small superconducting M - H loops up to 0.1 T (well below the upper critical
109 field H_{c2}) are presented in **Fig. 4b** and **Extended Data Fig. 6**.

110

111 **Superconducting T_c**

112 **Figure 5** summarises the discovered superconducting d^{9-x} nickel oxides under ambient pressure. The
113 present demonstration of a zero-resistance state above the 30 K range in SECS under ambient pressure
114 marks a new record. In addition, this is the first successful demonstration of superconductivity in the late
115 rare-earth (Sm) nickel oxides. This step of material expansion is critical to understanding the roles of rare
116 earth R 5d bands and R-Ni hybridization in the correlated orderings and pairing mechanism of nickelates,
117 whose uniqueness or universality would be the next question to address^{25,35}. Intriguingly, the trend in

superconducting T_c values from the earlier rare-earth (La/Pr/Nd)NiO₂ to the later rare earth Sm³⁺ in SECS does not simply correlate with the expected rare earth R³⁺ ionic size (or the resultant chemical pressure dependence): the largest difference is typically between La³⁺ and Pr³⁺/ Nd³⁺ ions, while the variation beyond Nd³⁺ for the even smaller rare earth ions is nearly negligible. Using the high- T_c iron pnictide superconductors as an example, the maximum bulk T_c of (R = La)[O_{1-x}F_x]FeAs is ~ 26 K (ref.⁵¹) while a much higher T_c is observed in the (R = Pr/Nd)[O_{1-x}F_x]FeAs between 52 – 53.5 K (ref.⁵²). Substituting the rare earth ions with smaller R (e.g., Sm) beyond Pr/Nd, however, does not increase the superconducting T_c considerably⁵². Unlike superconducting T_c , the normal state Hall coefficients R_H of RNiO₂ nickelates follow the expected rare earth dependence, in agreement with the shrinking rare earth electron pockets, especially after La (**Extended Data Fig. 7**). The maximum R_H sign-change temperature T_h is very low at ~ 30 K for the hole-doped LaNiO₂, and significantly higher $T_h > 100$ K for the hole-doped (Pr/Nd/Sm)NiO₂, including SECS (refs.^{17,46,47}). While the critical factors for higher superconducting T_c remain to be proposed and verified, it is plausible that the smaller Ca²⁺/Eu^{2+/3+} dopants might reduce the variance in the A-site ionic radii, leading to enhanced interlayer interactions or reduced A-site disorder⁴⁹ that is favourable for stronger superconducting pairing. In terms of material aspects, considering their bulk superconducting nature corroborated by the Meissner effect (complete field expulsion), further increase in superconducting T_c is likely possible in the clean bulk single crystal under ambient pressure, or under moderate applied hydrostatic pressure ~ 10 GPa where T_c enhancement effects were demonstrated⁵³.

136

137 **Outlook**

138 The demonstration of high- T_c superconductivity in SECS, together with the recently discovered $d^{7+\alpha}$ bilayer nickel oxides^{5,22}, enriches the high- T_c material platform as a high- T_c oxide-based layered 139 superconductor alternative to the cuprates^{1–4,15–19}. Comparing the observables between these two systems 140 should be highly valuable for determining the universal ingredient for unconventional high- T_c Cooper 141

pairing. Establishing the correlation between T_c and parameters (e.g., antiferromagnetic interaction J values, hopping, nuclear mass) may suggest a suitable interaction term for the Hubbard model description⁵⁴ and provide critical insight into the microscopic theory for the high- T_c Cooper pairing in the cuprates and nickelates. Considering the smaller antiferromagnetic J value in infinite-layer nickelates, which is about 1/3-1/2 of the cuprates, we note that the T_c of SECS is particularly large and comparable to those of single CuO₂ layer cuprates^{25,36-38}. While the superconducting T_c of cuprates negatively correlates with the magnitude of the charge transfer gap in their parent compounds⁵⁴, the charge transfer gap of infinite-layer nickelate is seemingly too large to support a superconducting T_c in the range of 40 K (refs.^{32,37}). Evidently, the present discovery should ignite momentum for theoretical and experimental investigations on the origin and pairing mechanism of this newfound high- T_c superconductivity without copper. This report paves the first step towards the understanding of and establishing a broad family of high-temperature unconventional superconducting layered oxides beyond cuprates.

154

155 References

1. Bednorz, J. G. & Müller, K. A. Possible high- T_c superconductivity in the Ba-La-Cu-O system. *Z. Phys. B* **64**, 189–193 (1986).
2. Maeno, Y. *et al.* Superconductivity in a layered perovskite without copper. *Nature* **372**, 532–534 (1994).
3. Takada, K. *et al.* Superconductivity in two-dimensional CoO₂ layers. *Nature* **422**, 53–55 (2003).
4. Li, D. *et al.* Superconductivity in an infinite-layer nickelate. *Nature* **572**, 624–627 (2019).
5. Sun, H. *et al.* Signatures of superconductivity near 80 K in a nickelate under high pressure. *Nature* **621**, 493–498 (2023).
6. Anderson, P. W. *et al.* The physics behind high-temperature superconducting cuprates: the plain vanilla version of RVB. *J. Phys. Condens. Matter* **16**, R755–R769 (2004).
7. Lee, P. A., Nagaosa, N. & Wen, X. G. Doping a Mott insulator: Physics of high-temperature superconductivity. *Rev. Mod. Phys.* **78**, 17–85 (2006).
8. Keimer, B., Kivelson, S. A., Norman, M. R., Uchida, S. & Zaanen, J. From quantum matter to high-temperature superconductivity in copper oxides. *Nature* **518**, 179–186 (2015).
9. Crespin, M., Levitz, P. & Gatineau, L. Reduced forms of LaNiO₃ perovskite. Part 1.—Evidence for new phases: La₂Ni₂O₅ and LaNiO₂. *J. Chem. Soc., Faraday Trans. 2* **79**, 1181–1194 (1983).
10. Hayward, M. A., Green, M. A., Rosseinsky, M. J. & Sloan, J. Sodium Hydride as a Powerful Reducing Agent for Topotactic Oxide Deintercalation: Synthesis and Characterization of the Nickel(I) Oxide LaNiO₂. *J. Am. Chem. Soc.* **121**, 8843–8854 (1999).

- 173 11. Zhou, G., Jiang, F., Zang, J., Quan, Z. & Xu, X. Observation of Superconductivity in the LaNiO₃/La_{0.7}Sr_{0.3}MnO₃
174 Superlattice. *ACS Appl. Mater. Interfaces* **10**, 1463–1467 (2018).
- 175 12. Zhang, J. *et al.* Large orbital polarization in a metallic square-planar nickelate. *Nat. Phys.* **13**, 864–869 (2017).
- 176 13. Rice, T. M. Electronic structure of possible nickelate analogs to the cuprates. *Phys. Rev. B - Condens. Matter Mater.*
177 *Phys.* **59**, 7901–7906 (1999).
- 178 14. Lee, K. W. & Pickett, W. E. Infinite-layer LaNiO₂: Ni¹⁺ is not Cu²⁺. *Phys. Rev. B - Condens. Matter Mater. Phys.* **70**,
179 1–7 (2004).
- 180 15. Pan, G. A. *et al.* Superconductivity in a quintuple-layer square-planar nickelate. *Nat. Mater.* **21**, 160–164 (2022).
- 181 16. Zeng, S. *et al.* Superconductivity in infinite-layer nickelate La_{1-x}Ca_xNiO₂ thin films. *Sci. Adv.* **8**, eabl9927 (2022).
- 182 17. Osada, M., Wang, B. Y., Lee, K., Li, D. & Hwang, H. Y. Phase diagram of infinite layer praseodymium nickelate Pr_{1-x}Sr_xNiO₂ thin films. *Phys. Rev. Mater.* **4**, 1–5 (2020).
- 184 18. Osada, M. *et al.* Nickelate Superconductivity without Rare-Earth Magnetism: (La,Sr)NiO₂. *Adv. Mater.* **33**, 1–7 (2021).
- 185 19. Wei, W., Vu, D., Zhang, Z., Walker, F. J. & Ahn, C. H. Superconducting Nd_{1-x}Eu_xNiO₂ thin films using in situ synthesis. *Sci. Adv.* **9**, (2023).
- 187 20. Sahib, H. *et al.* Superconductivity in PrNiO₂ infinite-layer nickelates. *arXiv* 2410.16147 (2024).
- 188 21. Parzyck, C. T. *et al.* Superconductivity in the parent infinite-layer nickelate NdNiO₂. *arXiv* 2410.02007 (2024).
- 189 22. Ko, E. K. *et al.* Signatures of ambient pressure superconductivity in thin film La₃Ni₂O₇. *Nature* **638**, 935–940 (2025).
- 190 23. Parzyck, C. T. *et al.* Absence of 3a0 charge density wave order in the infinite-layer nickelate NdNiO₂. *Nat. Mater.* **23**,
191 486–491 (2024).
- 192 24. Krieger, G. *et al.* Charge and Spin Order Dichotomy in NdNiO₂ Driven by the Capping Layer. *Phys. Rev. Lett.* **129**,
193 27002 (2022).
- 194 25. Rossi, M. *et al.* Universal orbital and magnetic structures in infinite-layer nickelates. *Phys. Rev. B* **109**, 024512 (2024).
- 195 26. Chow, L. E. *et al.* Pauli-limit violation in lanthanide infinite-layer nickelate superconductors. *arXiv* 2204.12606 (2022).
- 196 27. Wang, B. Y. *et al.* Effects of rare-earth magnetism on the superconducting upper critical field in infinite-layer nickelates. *Sci. Adv.* **9**, (2023).
- 198 28. Wang, B. Y. *et al.* Isotropic Pauli-limited superconductivity in the infinite-layer nickelate Nd_{0.775}Sr_{0.225}NiO₂. *Nat. Phys.* **17**, 473–477 (2021).
- 200 29. Chow, L. E. *et al.* Pairing symmetry in infinite-layer nickelate superconductor. *arXiv* 2201.10038 (2022).
- 201 30. Harvey, S. P. *et al.* Evidence for nodal superconductivity in infinite-layer nickelates. *arXiv* 2201.12971 (2022).
- 202 31. Chow, L. E. & Ariando, A. Infinite-Layer Nickelate Superconductors: A Current Experimental Perspective of the
203 Crystal and Electronic Structures. *Front. Phys.* **10**, 1–8 (2022).
- 204 32. Wang, B. Y., Lee, K. & Goodge, B. H. Experimental Progress in Superconducting Nickelates. *Annu. Rev. Condens.*
205 *Matter Phys.* **15**, 305–324 (2024).
- 206 33. Held, K. *et al.* Phase Diagram of Nickelate Superconductors Calculated by Dynamical Vertex Approximation. *Front.*
207 *Phys.* **9**, (2022).
- 208 34. Karp, J. *et al.* Many-Body Electronic Structure of NdNiO₂ and CaCuO₂. *Phys. Rev. X* **10**, 1–28 (2020).
- 209 35. Foyevtsova, K., Elfimov, I. & Sawatzky, G. A. Distinct electridelike nature of infinite-layer nickelates and the resulting
210 theoretical challenges to calculate their electronic structure. *Phys. Rev. B* **108**, 205124 (2023).
- 211 36. Hepting, M., Dean, M. P. M. & Lee, W. S. Soft X-Ray Spectroscopy of Low-Valence Nickelates. *Front. Phys.* **9**, 1–9
212 (2021).
- 213 37. Nomura, Y. & Arita, R. Superconductivity in infinite-layer nickelates. *Reports Prog. Phys.* **85**, 052501 (2022).

- 214 38. Been, E. M. *et al.* On the Nature of Valence Charge and Spin Excitations via Multi-Orbital Hubbard Models for Infinite-
215 Layer Nickelates. *Front. Phys.* **10**, 1–7 (2022).
- 216 39. Hepting, M. *et al.* Electronic structure of the parent compound of superconducting infinite-layer nickelates. *Nat. Mater.*
217 **19**, 381–385 (2020).
- 218 40. Zhang, R. *et al.* Magnetic and f-electron effects in LaNiO_2 and NdNiO_2 nickelates with cuprate-like $3d_{x^2-y^2}$ band.
219 *Commun. Phys.* **4**, 1–12 (2021).
- 220 41. Lechermann, F. Emergent flat-band physics in $d^{9-\delta}$ multilayer nickelates. *Phys. Rev. B* **105**, (2022).
- 221 42. Armitage, N. P., Fournier, P. & Greene, R. L. Progress and perspectives on electron-doped cuprates. *Rev. Mod. Phys.*
222 **82**, 2421–2487 (2010).
- 223 43. Wang, Z., Zhang, G. M., Yang, Y. F. & Zhang, F. C. Distinct pairing symmetries of superconductivity in infinite-layer
224 nickelates. *Phys. Rev. B* **102**, 1–6 (2020).
- 225 44. Bandyopadhyay, S., Adhikary, P., Das, T., Dasgupta, I. & Saha-Dasgupta, T. Superconductivity in infinite-layer
226 nickelates: Role of f orbitals. *Phys. Rev. B* **102**, 1–6 (2020).
- 227 45. Chow, L. E. *et al.* Dimensionality control and rotational symmetry breaking superconductivity in square-planar layered
228 nickelates. *arXiv:2301.07606* (2023).
- 229 46. Li, D. *et al.* Superconducting Dome in $\text{Nd}_{1-x}\text{Sr}_x\text{NiO}_2$ Infinite Layer Films. *Phys. Rev. Lett.* **125**, 027001 (2020).
- 230 47. Zeng, S. *et al.* Phase Diagram and Superconducting Dome of Infinite-Layer $\text{Nd}_{1-x}\text{Sr}_x\text{NiO}_2$ Thin Films. *Phys. Rev. Lett.*
231 **125**, 147003 (2020).
- 232 48. Bernardini, F., Bosin, A. & Cano, A. Geometric effects in the infinite-layer nickelates. *Phys. Rev. Mater.* **6**, 044807
233 (2022).
- 234 49. Attfield, J. P., Kharlanov, A. L. & McAllister, J. A. Cation effects in doped La_2CuO_4 superconductors. *Nature* **394**, 157–
235 159 (1998).
- 236 50. Lee, Y. *et al.* Synthesis of superconducting freestanding infinite-layer nickelate heterostructures on the millimetre scale.
237 *Nat. Synth* (2025). <https://doi.org/10.1038/s44160-024-00714-2>.
- 238 51. Kamihara, Y., Watanabe, T., Hirano, M. & Hosono, H. Iron-Based Layered Superconductor $\text{La}[\text{O}_{1-x}\text{F}_x]\text{FeAs}$
239 ($x=0.05\text{--}0.12$) with $T_c = 26$ K. *J. Am. Chem. Soc.* **130**, 3296–3297 (2008).
- 240 52. Ren, Z.-A. *et al.* Superconductivity and phase diagram in iron-based arsenic-oxides $\text{ReFeAsO}_{1-\delta}$ (Re = rare-earth metal)
241 without fluorine doping. *EPL (Europhysics Lett.)* **83**, 17002 (2008).
- 242 53. Wang, N. N. *et al.* Pressure-induced monotonic enhancement of T_c to over 30 K in superconducting $\text{Pr}_{0.82}\text{Sr}_{0.18}\text{NiO}_2$ thin
243 films. *Nat. Commun.* **13**, 2–6 (2022).
- 244 54. Wang, Z. *et al.* Correlating the charge-transfer gap to the maximum transition temperature in $\text{Bi}_2\text{Sr}_2\text{Ca}_{n-1}\text{Cu}_n\text{O}_{2n+4+\delta}$.
245 *Science* **381**, 227–231 (2023).
- 246 55. Cava, R. J. *et al.* Superconductivity near 30 K without copper: the $\text{Ba}_{0.6}\text{K}_{0.4}\text{BiO}_3$ perovskite. *Nature* **332**, 814–816 (1988).
- 247 56. Wu, M. K. *et al.* Superconductivity at 93 K in a new mixed-phase Yb-Ba-Cu-O compound system at ambient pressure.
248 *Phys. Rev. Lett.* **58**, 908–910 (1987).
- 249 57. Schilling, A., Cantoni, M., Guo, J. D. & Ott, H. R. Superconductivity above 130 K in the Hg–Ba–Ca–Cu–O system.
250 *Nature* **363**, 56–58 (1993).
- 251 58. Sleight, A. W., Gillson, J. L. & Bierstedt, P. E. High-temperature superconductivity in the $\text{BaPb}_{1-x}\text{Bi}_x\text{O}_3$ systems. *Solid
252 State Commun.* **17**, 27–28 (1975).
- 253
- 254
- 255

256 **Main Figure Legends**

257 **Fig. 1 | Structural information on the superconducting SECS nickel oxide thin films.** **a**, Schematic diagram for
258 the crystal structure of SECS infinite-layer nickelate. **b**, X-ray diffraction θ - 2θ symmetric scan of a representative
259 $\text{Sm}_{0.79}\text{Eu}_{0.12}\text{Ca}_{0.04}\text{Sr}_{0.05}\text{NiO}_2$ thin film. **c**, Cross-sectional STEM-HAADF image shows a large area of infinite-layer
260 lattice without structural RP-type defects.

261

262 **Fig. 2 | Transport characteristics of the superconducting SECS nickel oxide thin films.** **a**,
263 $\text{Sm}_{0.79}\text{Eu}_{0.12}\text{Ca}_{0.04}\text{Sr}_{0.05}\text{NiO}_2$ (the lowest resistivity sample). **b**, $\text{Sm}_{0.75}\text{Eu}_{0.2}\text{Ca}_{0.05}\text{NiO}_2$ (the highest superconducting T_c
264 sample). **c**, The largest superconducting doping $\text{Sm}_{0.74}\text{Eu}_{0.06}\text{Ca}_{0.01}\text{Sr}_{0.19}\text{NiO}_2$ sample. The resistivity curves exhibit T -
265 linear behaviour at high temperatures and positive curvatures at temperatures below ~ 100 K (fitted to $\rho = \rho_0 +$
266 AT^n , $1 < n < 2$) until the superconducting transition where the resistivity drops.

267

268 **Fig. 3 | Zero resistance and diamagnetic state in the SECS nickel oxide thin film.** **a**, Resistivity $\rho(T)$ curve of
269 the representative $\text{Sm}_{0.75}\text{Eu}_{0.2}\text{Ca}_{0.05}\text{NiO}_2$ sample shows superconducting transition with zero resistance observed at
270 31 K. **b**, DC susceptibility measurement shows a substantial diamagnetism below ~ 27 K, which is below the
271 resistivity transition temperature due to the thin film geometry. The paramagnetic contribution from the NGO
272 substrate is subtracted, where the raw data is shown in the **Extended Data Fig. 5**.

273

274 **Fig. 4 | Meissner state in the nickel oxide thin films.** **a**, Meissner state is evidenced from the linear negative slope
275 observed in the field-dependence susceptibility curve near zero applied field, demonstrating complete field expulsion
276 in the representative $\text{Sm}_{0.75}\text{Eu}_{0.2}\text{Ca}_{0.05}\text{NiO}_2$ thin film shown in Fig. 3. **b**, Superconducting M - H loops at several
277 temperatures.

278

279 **Fig. 5 | Discoveries of superconducting d^{9-x} nickel oxides.** The infinite-layer nickelates family $(\text{R}, \text{A})\text{NiO}_2$, where
280 $\text{R} = \text{La}, \text{Pr}, \text{Nd}, \text{Sm}$ and dopant $\text{A} = \text{Sr}, \text{Ca}, \text{Eu}$, are labelled by their A-site elements (R, A) . **a**, Resistivity-
281 temperature $\rho(T)$ curves of the infinite-layer nickelates (first reported)^{4,16–19}. The curves are vertically shifted for
282 clarity. **b**, Discoveries of superconducting oxides and their T_c at ambient pressure^{1–4,15–19,55–58}.

283

284

285 **Methods**

286 **Sample growth and preparation**

287 The superconducting infinite-layer nickelate $\text{Sm}_{1-x-y-z}\text{Eu}_x\text{Ca}_y\text{Sr}_z\text{NiO}_2$ (SECS) thin films were synthesized
288 on NdGaO_3 (110) or NGO substrates using pulsed laser deposition (PLD) followed by a topotactic
289 reduction process in a vacuum chamber. We note that oxygen off-stoichiometry $\text{ANiO}_{2+\delta}$ is likely in
290 general; however, for simplicity, we use the stoichiometric formula ANiO_2 throughout this manuscript.
291 Similarly, oxygen vacancy may form in the as grown Ruddlesden–Popper perovskite phase ANiO_{3-y} (refer
292 to Supplementary Information Figs. S4,S5 for their structural and transport characterisation); we use the
293 stoichiometric formula ANiO_3 . NdGaO_3 (110) substrates (Shinkosha) were pre-annealed at 1,050°C for 4
294 hours in air to achieve a single-termination surface¹⁵. This choice of substrate ($\sim 3.86\text{--}3.87 \text{ \AA}$) is to better
295 match the lattice constant of infinite-layer SmNiO_2 ($\sim 3.88 \text{ \AA}$, $\sim 3.87 \text{ \AA}$ for EuNiO_2)⁴⁸. The reduced
296 infinite-layer phase is nearly strain-free, while the perovskite phase has a tensile strain of around +2.2%.
297 Considering the lower thermodynamic stability of the hole-doped late rare-earth perovskite nickelate
298 compared to those of larger rare-earth elements or undoped perovskites, we focus on a thickness of
299 approximately 10-20 uc for the perovskite films³¹, which were deposited at a growth temperature of
300 $T_{growth} = 615^\circ\text{C}\text{--}625^\circ\text{C}$ and an oxygen pressure of $P_{O_2} = 200 \text{ mTorr}$, with a laser fluence of 2.3-2.7
301 Jcm^{-2} at 1 Hz using a shadow mask (refer to Supplementary Information Fig. S6 for STEM-HAADF
302 characterization of $\text{Sm}_{0.74}\text{Eu}_{0.06}\text{Ca}_{0.01}\text{Sr}_{0.19}\text{NiO}_2$ thin film synthesized under preliminary growth conditions
303 without a shadow mask). An additional advantage of a thinner sample is easier control over the phase
304 homogeneity³¹. After deposition, samples were *in-situ* capped with epitaxial SrTiO_3 of $\sim 1 \text{ nm}$ (thickness
305 varies with day-to-day fluctuations in laser collimation) using a low laser fluence $\sim 0.6 \text{ Jcm}^{-2}$ (ref.⁵⁹). The
306 topotactic reduction temperature is between 300°C–325°C (ref.⁶⁰), with a total annealing duration of
307 between 2-6 hours to achieve a sufficiently low resistivity below $\sim 2 \text{ m}\Omega \cdot \text{cm}$ or until a maximum
308 superconducting T_c is observed.

310 **X-ray diffraction**

311 The X-ray diffraction (XRD) $\theta\text{-}2\theta$ symmetric scan was done in the X-ray Diffraction and Development
312 (XDD) beamline at the Singapore Synchrotron Light Source (SSLS) with an X-ray wavelength of $\lambda =$
313 1.5404 \AA .

315 **Scanning transmission electron microscopy**

316 The thin film samples were first capped with gold or platinum prior to the lamella preparation. A focused
317 ion beam (FIB) instrument (FEI Versa 3D) operated at 30 kV was used to prepare cross-sectional lamellae
318 of the nickelate thin films. Subsequently, cleaning at 2 kV was performed to remove the amorphous surface
319 layer. The scanning transmission electron microscopy (STEM) characterization was conducted on a
320 JEMARM200F (JEOL) microscope operated at 200 kV and equipped with a cold field emission gun and a
321 Cs-probe aberration corrector. High-angle annular dark-field (HAADF) images were acquired using inner
322 and outer collection semi-angles of about 70 and 280 mrad, respectively, with a convergence semi-angle
323 of about 30 mrad.

324

325 **Transport characterization**

326 The wire connection for the electrical transport measurement was made using Al ultrasonic wire bonding.
327 The contact resistance is typically a few hundred Ohms. The longitudinal and Hall transport measurements
328 at temperatures down to 2 K and magnetic fields up to 9 T were performed using a Quantum Design
329 Physical Property Measurement System. Zero resistance $T_{c,0}$ is defined as the temperature at which the
330 resistivity reaches zero (below the measurement limit $\sim < 0.001 \Omega$ or $\sim 10^{-9} \Omega \cdot m$ for the few nm thin
331 films). The onset of superconductivity $T_{c,onset}$ is defined as the temperature where $\frac{\partial^2 \rho}{\partial T^2}$ drops below zero⁵⁹.
332 The 90% transition temperature $T_{c,90\%}$ is defined as the temperature where resistivity drops to 90% of the
333 normal state resistivity defined as $\rho(\max \text{ of } T_{c,onset} \rightarrow 40 \text{ K})$ ⁴⁶ except for the underdoped
334 Sm_{0.85}Eu_{0.06}Ca_{0.08}Sr_{0.01}NiO₂ thin film (refer to Supplementary Information Fig. S7 for their $T_{c,onset}$).
335

336 **Susceptibility measurement**

337 The Meissner state of the superconducting thin film was detected through DC susceptibility measurements
338 using a Quantum Design Superconducting Quantum Interference Device Magnetometer. We applied a
339 small DC field of < 10 Oe along the $H \parallel c$ the direction, perpendicular to the thin film plane. The NGO
340 substrate contributes a paramagnetic background signal, which was subtracted from the M - T loop using a
341 linear fit. The M - T curve presented in the main text has the paramagnetic background subtracted using the
342 Curie-Weiss law (refer to Supplementary Information Fig. S3), where the raw data are presented in the
343 **Extended Data Fig. 5**. A clear superconducting transition can be observed in the raw M - T curves.

344

345 **Methods Reference**

346 59. Lee, K. *et al.* Linear-in-temperature resistivity for optimally superconducting (Nd,Sr)NiO₂. *Nature* **619**, 288–292 (2023).

347 60. Balakrishnan, P.P. *et al.* Extensive hydrogen incorporation is not necessary for superconductivity in topotactically reduced
348 nickelates. *Nat Commun* **15**, 7387 (2024).

349

350 **Acknowledgement**

351 This research is supported by the Ministry of Education (MOE), Singapore, under its Tier-2 Academic
352 Research Fund (AcRF), Grant No. MOE-T2EP50121-0018 and MOE-T2EP50123-0013, by the MOE Tier-
353 3 Grant (MOE-MOET32023-0003) 'Quantum Geometric Advantage', and by the SUSTech-NUS Joint
354 Research Program. S.L.E.C. acknowledges support from the President's Graduate Fellowship provided by
355 the National University of Singapore. The authors would also like to acknowledge the Singapore
356 Synchrotron Light Source (SSLS) for providing the facility necessary for conducting the research. The
357 laboratory is a National Research Infrastructure under the National Research Foundation (NRF) Singapore.
358 We thank the technical supports from Qian He, Yang Ping, Ngee Hong Teo, Shengwei Zeng, Zhi Shiu
359 Lim, Saurav Prakash, and Xing Gao. We acknowledge useful discussions with George Sawatzky, Danfeng
360 Li, Kazuhiko Kuroki, Hans J.W.M. Hilgenkamp, Frank Lechermann, Yi-Feng Yang, Yijun Yu, Bai Yang
361 Wang, Kyuho Lee, Dan Ferenc Segedin, Hariom Jani, and Wenzheng Wei.

362

363 **Author information**

364 **Authors and Affiliations**

365 **1. Department of Physics, National University of Singapore, Singapore 117551, Singapore.**

366 S. Lin Er Chow, Zhaoyang Luo, A. Ariando

367

368 **Author contributions**

369 S.L.E.C. and A.A. conceived the project and designed the experiments. S.L.E.C. synthesized the nickelate
370 films, conducted the transport characterization, and performed the susceptibility measurements. Z.L.
371 conducted the structural analysis. All authors analysed and discussed the data. S.L.E.C. and A.A. wrote the
372 manuscript. A.A. secured the grants and led the “superconductivity” programs at the National University
373 of Singapore.

374

375 **Corresponding author**

376 Correspondence to S. Lin Er Chow (le.chow@u.nus.edu), or A. Ariando (ariando@nus.edu.sg)

377

378 **Competing interests**

379 The authors declare no competing interests.

380

381 **Data availability**

382 The data that support the findings of this study are provided in the manuscript and supplementary
383 information. All other relevant data are available from the corresponding authors.

384

385

386 **Extended Data Figure Captions**

387 **Extended Data Fig. 1 | Low-magnification STEM-HAADF and Fast-Fourier-Transform (FFT)**
388 **images of the representative superconducting $\text{Sm}_{0.79}\text{Eu}_{0.12}\text{Ca}_{0.04}\text{Sr}_{0.05}\text{NiO}_2$ thin film.**

389 **Extended Data Fig. 2 | Additional STEM-HAADF images show several areas of the representative**
390 **$\text{Sm}_{0.79}\text{Eu}_{0.12}\text{Ca}_{0.04}\text{Sr}_{0.05}\text{NiO}_2$ thin film.** The infinite-layer film is virtually free of RP-type structural defects.

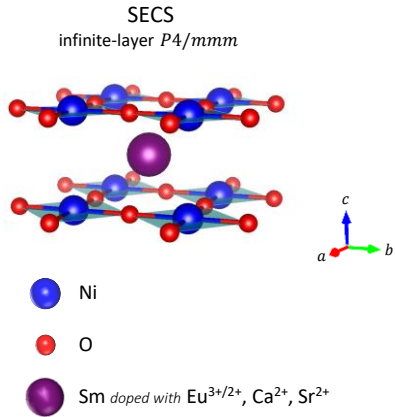
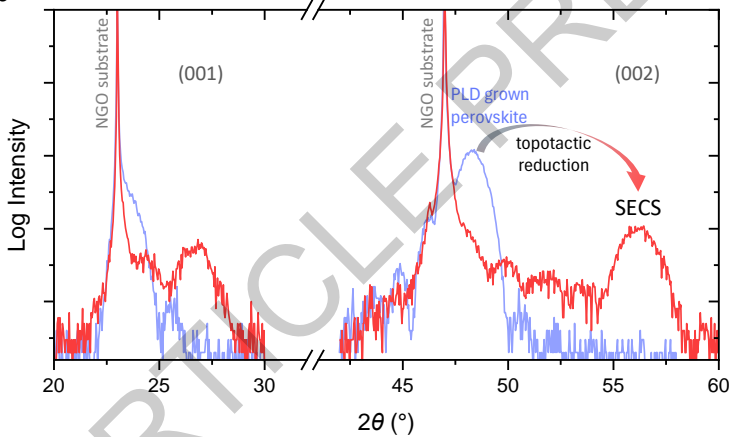
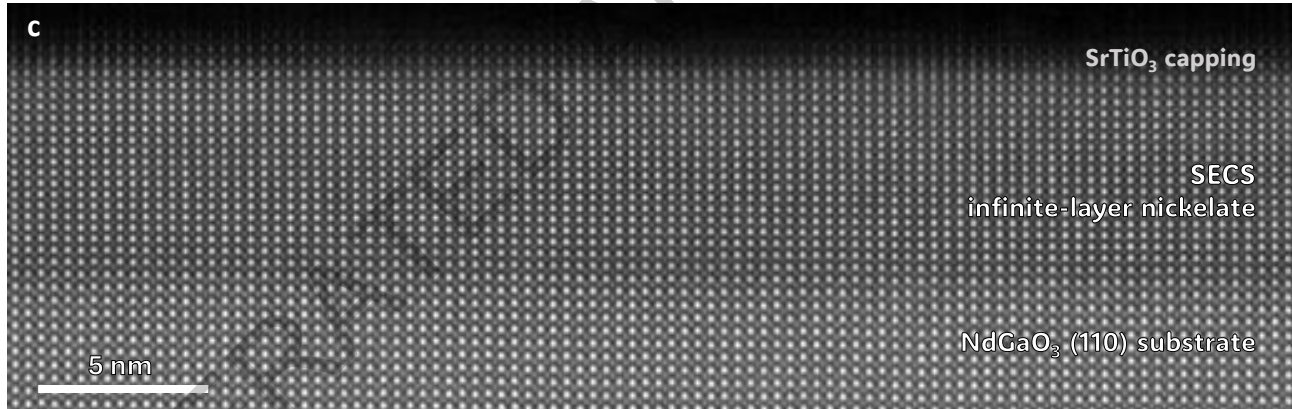
391 **Extended Data Fig. 3 | Curvature of the resistivity $\rho(T)$ curve $\frac{\partial^2 \rho}{\partial T^2}$ in Fig. 2b.** The superconducting
392 transition ends with zero resistance state at 31 K. Inset shows the magnification of the $\frac{\partial^2 \rho}{\partial T^2}$ near the onset.

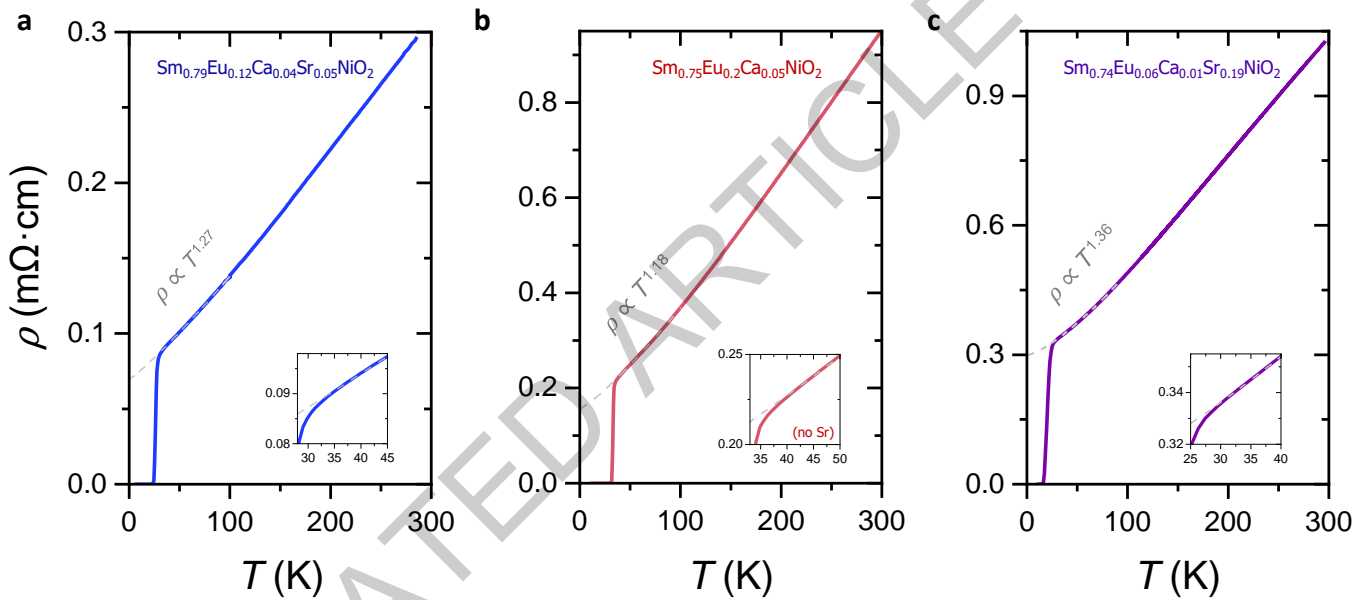
393 **Extended Data Fig. 4 | Comparison of the resistivity $\rho(T)$ curves between different dopant**
394 **concentrations. a,** $\text{Sm}_{0.73}\text{Eu}_{0.2}\text{Ca}_{0.07}\text{NiO}_2$ ($h = 0.19$) with $T_{c,0} = 26.5$ K. **b,** $\text{Sm}_{0.53}\text{Eu}_{0.4}\text{Ca}_{0.07}\text{NiO}_2$ ($h =$
395 0.31) which is outside of superconducting phase. The overdoped $\text{Sm}_{0.53}\text{Eu}_{0.4}\text{Ca}_{0.07}\text{NiO}_2$ is completely
396 metallic at all temperatures, with a low residual resistivity $\rho_0 = 0.0108 \text{ m}\Omega \cdot \text{cm}$ and a residual-resistivity-
397 ratio RRR ~ 10 .

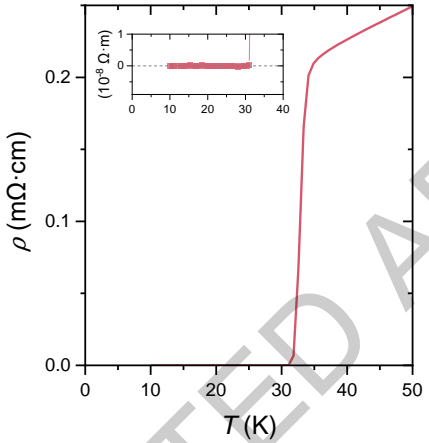
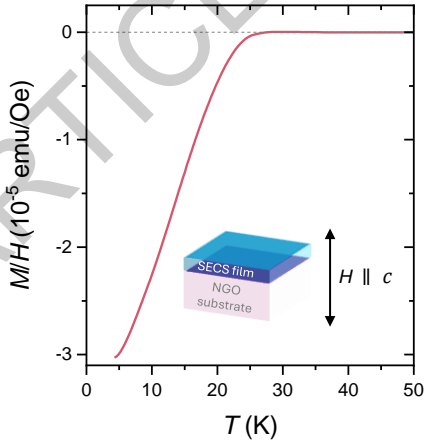
398 **Extended Data Fig. 5 | Raw M - T data measured at applied field $H \parallel c = 2, 9, 3.6, 9.7 \text{ Oe}$ of a**
399 **representative $\text{Sm}_{0.75}\text{Eu}_{0.2}\text{Ca}_{0.05}\text{NiO}_2$ thin film.**

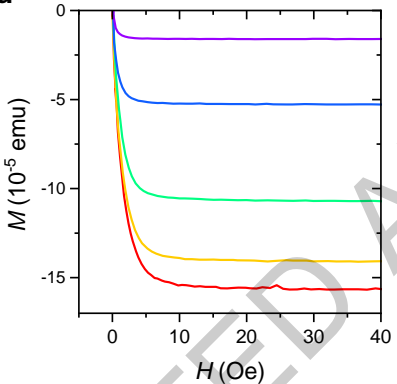
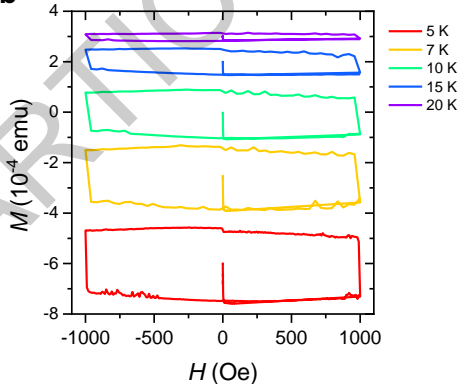
400 **Extended Data Fig. 6 | Small superconducting M - H loops of the representative $\text{Sm}_{0.75}\text{Eu}_{0.2}\text{Ca}_{0.05}\text{NiO}_2$**
401 **thin film shown in Fig. 3 with diamagnetism observed below ~ 27 K.**

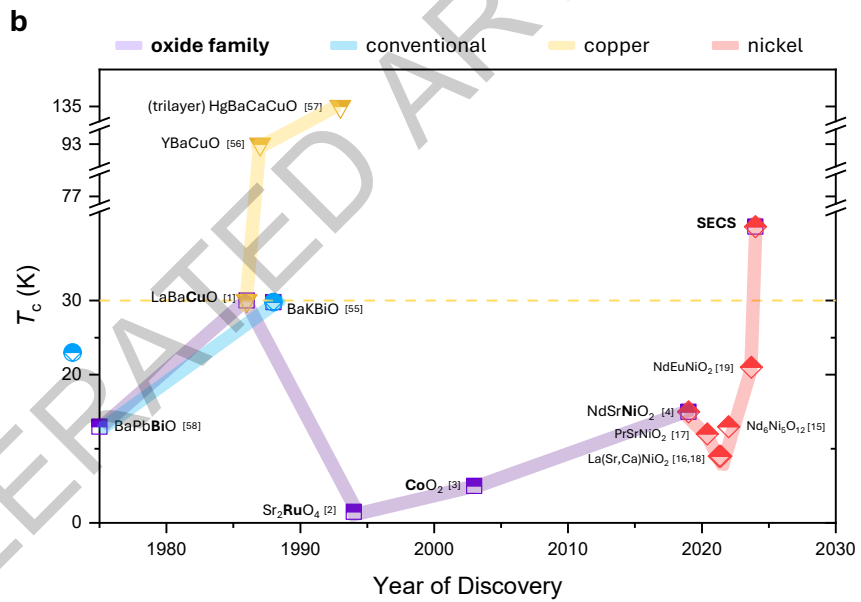
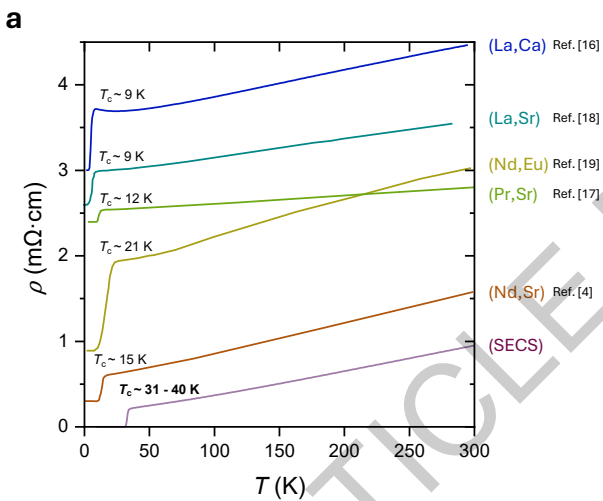
402 **Extended Data Fig. 7 | Normal state Hall coefficients of SECS thin films. a,** Hall coefficients *vs*
403 temperature $R_H(T)$ plot. **b,** Majority holes *vs* electrons phase diagram of various infinite-layer nickelates
404 $(R, A)\text{NiO}_2$ showing R_H sign crossover temperature T_h as a function of hole doping, adapted from refs.¹⁶⁻
405 ^{18,59}. For $\text{Sm}_{1-x-y-z}\text{Eu}_x\text{Ca}_y\text{Sr}_z\text{NiO}_2$, hole doping is estimated as $h = 0.6x + y + z$ (ref.¹⁹). **c,** Maximum T_h
406 as a function of rare earth ions (R) from La – Sm.

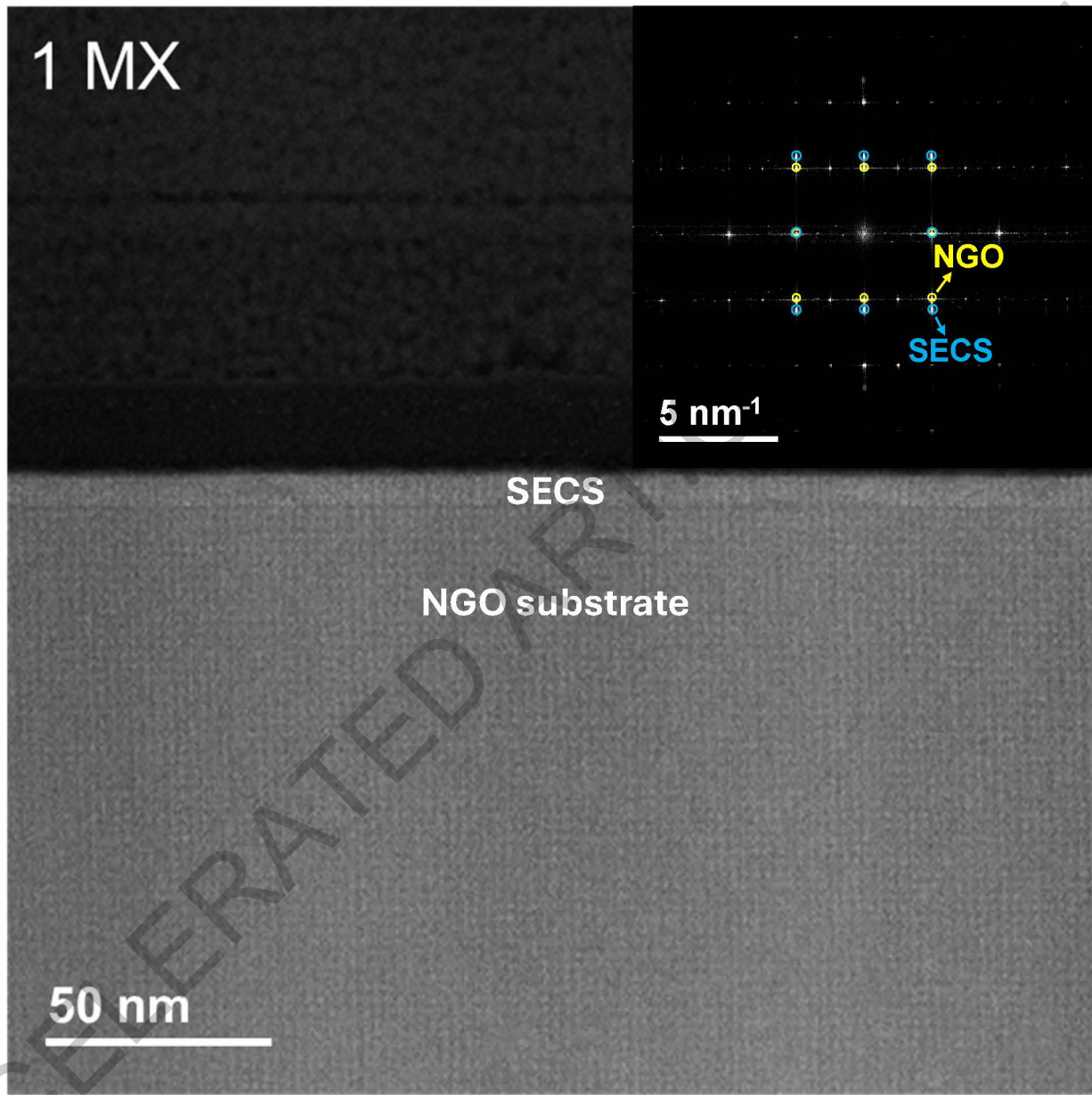
a**b****c**



a**b**

a**b**

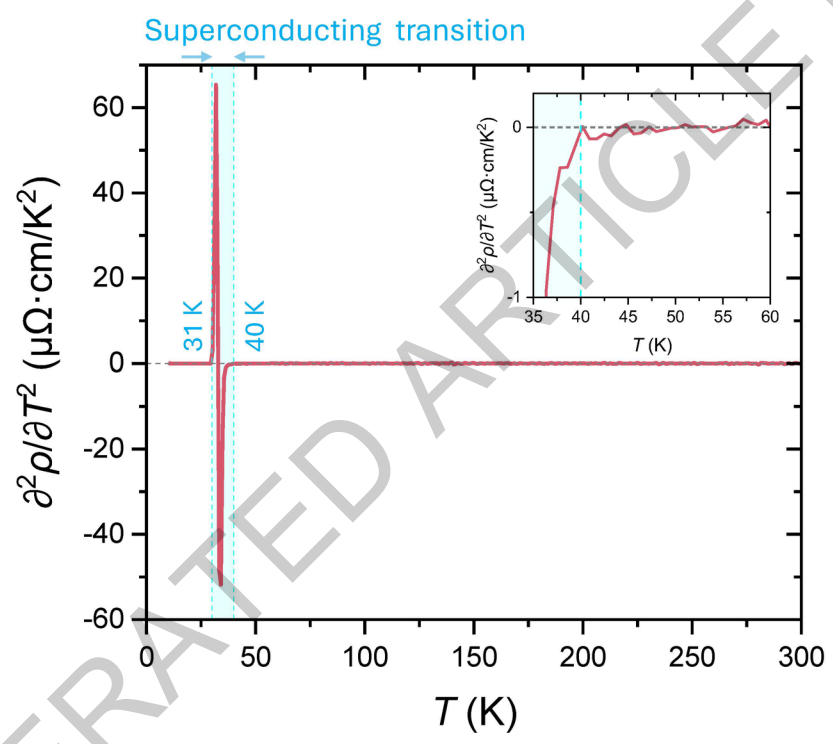




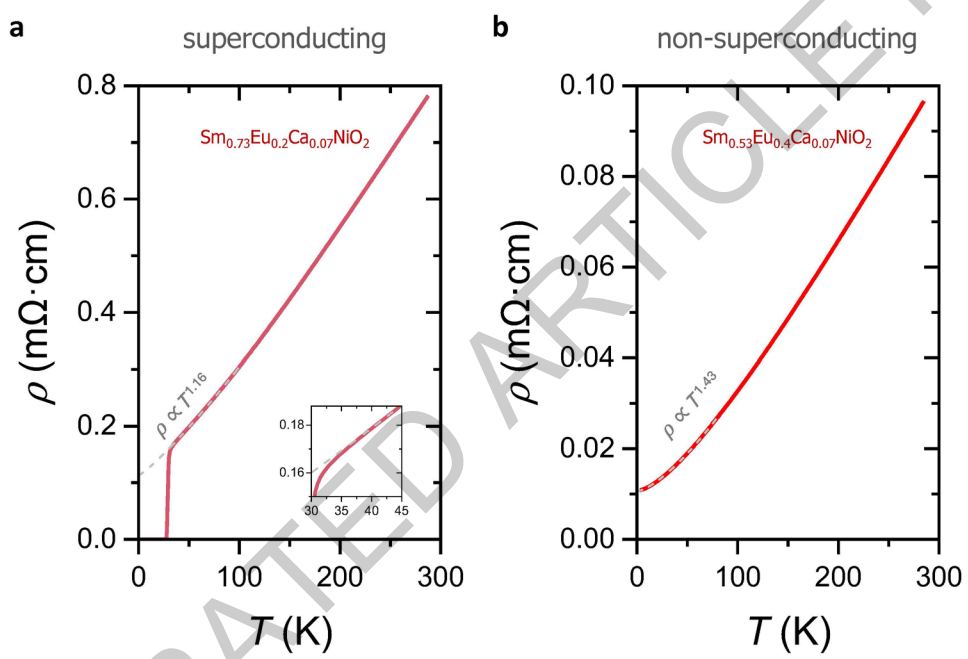
Extended Data Fig. 1



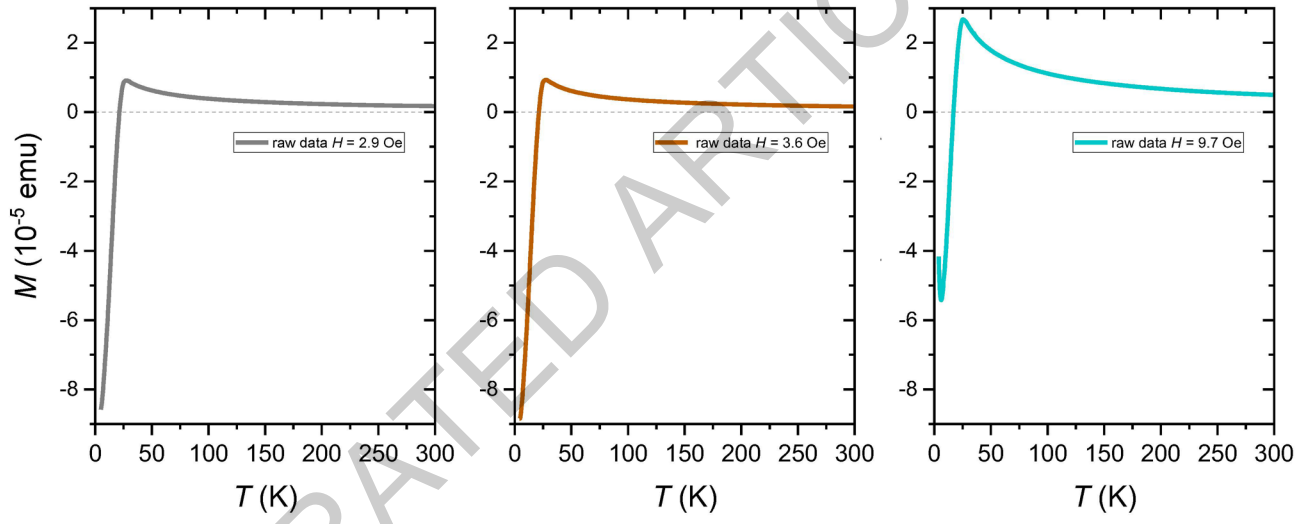
Extended Data Fig. 2



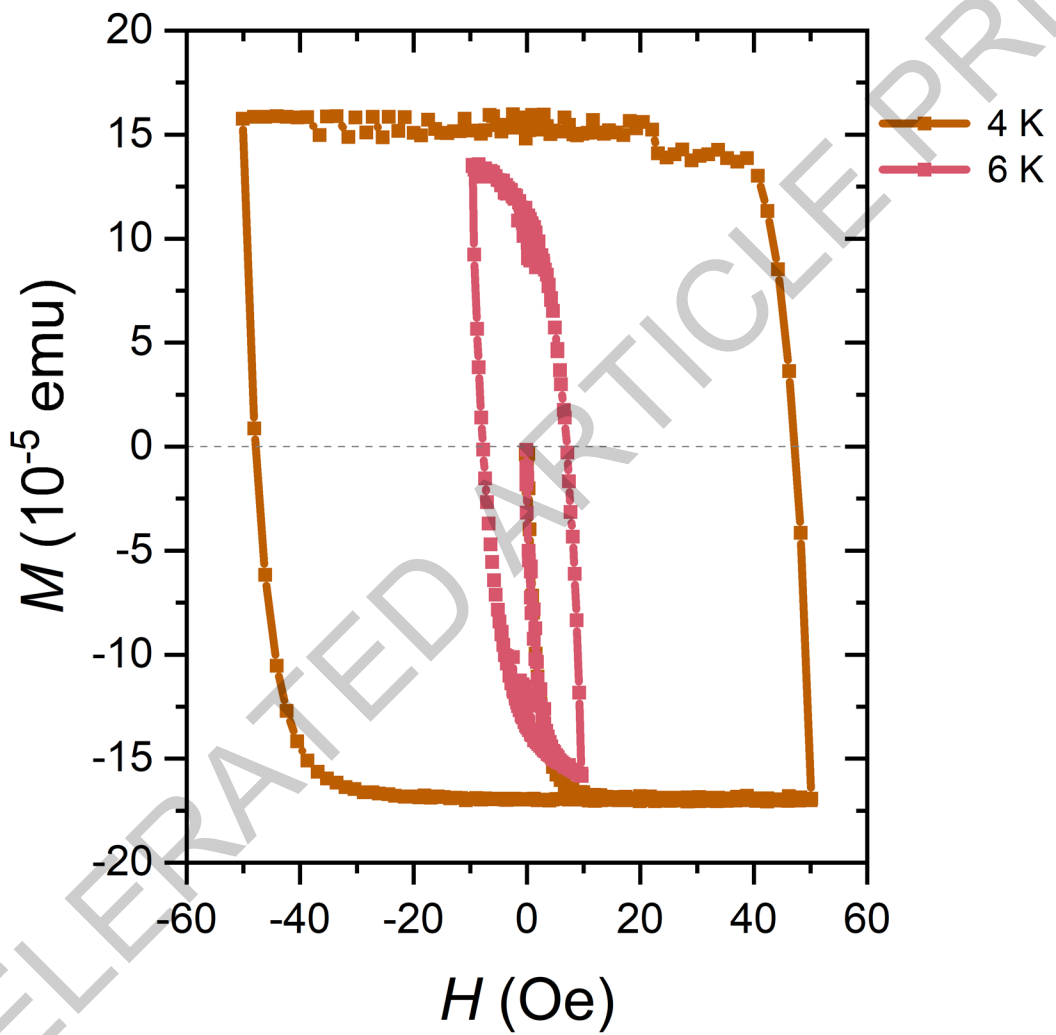
Extended Data Fig. 3



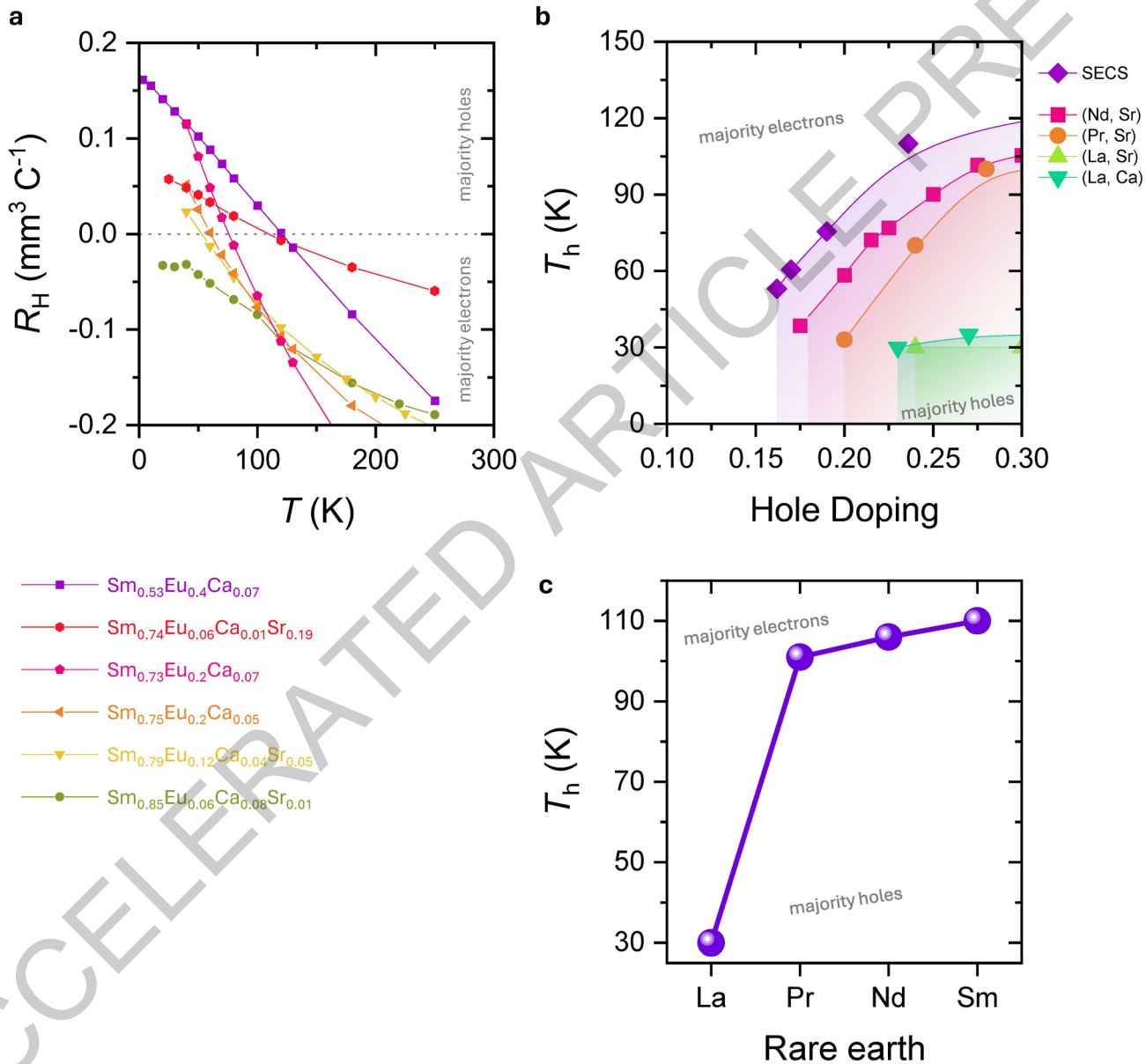
Extended Data Fig. 4



Extended Data Fig. 5



Extended Data Fig. 6



Extended Data Fig. 7